Investigating the Scattering Characteristics of Artificial Field-Aligned Irregularities Based on T-Matrix Algorithm

Shuai S. A. Yuan, *Graduate Student Member, IEEE*, Zhu Hong Lin, Li-Bin Lv, Shu-Ji Hao, and Wei E. I. Sha, *Senior Member, IEEE*

***Abstract*—The artificial field-aligned irregularity (AFAI) in ionosphere can be generated by heating the ionosphere with high-power high-frequency radio waves, and the physical structures of AFAIs are modeled as elongated multiple multilayer plasma cylinders. At relatively low frequencies, AFAIs could work as natural reflectors for long-distance communications. In order to evaluate the performance of AFAI-based communications, it is crucial to obtain the objective radar cross section (RCS) of AFAIs quickly and accurately. On account of the large electrical size of AFAIs, it would be time-consuming to calculate the objective RCS by full-wave simulations, meanwhile, the accuracies of the existing approximated methods are limited in many scenarios. In this paper, the T-matrix algorithm is used for analytically calculating the objective RCS of AFAIs after making reasonable approximations. Compared to the results obtained from full-wave simulations, the errors of objective RCS are within an acceptable range while the computation time is largely reduced. Furthermore, the scattering characteristics of AFAIs at different frequencies are investigated. The proposed method could be readily implemented for investigating and predicting the performance of AFAI-based long-wave communications.**

***Index Terms*—T-matrix algorithm, artificial field-aligned irregularities, ionospheric long-wave communications, generalized reflection coefficients, Scattering characteristics.**

I. Introduction

THE ionosphere can reflect low-frequency electromagnetic waves to realize ultra-long-distance communications, which has great values in scientific researches and engineering applications [1], [2], [3]. Since the 1970 s, the experiments of heating the ionosphere with high-power high-frequency radio waves have drawn extensive attentions [4], [5], [6], [7]. After heating the ionosphere, the plasma irregularities with inhomogeneous electron density distributed along the geomagnetic field can be produced near the reflecting height of the ionosphere [8], [9], [10], and the size of a single irregularity usually ranges from several meters to tens of meters [11], [12]. Due to the characteristic of distributing along the geomagnetic field, the plasma irregularity is called artificial field-aligned irregularity (AFAI) [9], [13]. Compared to the background ionosphere, the electron density of AFAI is higher, which indicates a higher plasma cutoff frequency. Therefore, AFAIs are expected to improve the performance and broaden the frequency range of ionospheric long-wave communications [14]. Experimental observations of AFAIs mainly include the Platteville heating station [4], the HIPAS heating station [15], the Sura heating station [16] and the HAARP heating station [17], etc. The theoretical analyses of AFAIs include the generating mechanism [6], [7], [12] and the scattering characteristics of AFAIs [18], [19], [20]. Recently, many researches on the experimental detection, physical characteristics and numerical simulations of AFAIs are conducted [16], [21], [22], [23], [24], laying the theoretical and experimental foundations of ionospheric AFAI-based long-wave communications.

Since AFAIs work as reflectors for long-wave communications, calculating the radar cross section (RCS) of the given AFAIs quickly and accurately is of great importance. The specific value of the objective RCS of AFAIs is directly related to the communication quality. Due to the large electrical size of AFAIs, full-wave simulations (such as finite-difference time-domain methods) will take too much time and require large computer memory [25], [26], [27]. The accuracies of some approximation methods in different scenarios are restricted [21], [28]. Regarding that the physical shapes of AFAIs are close to elongated cylinders, the objective RCS of AFAIs can be approximately estimated after making some reasonable approximations. We first analytically calculate the two-dimensional (2-D) radar scattering width of the infinitely-long cylinders with the same radii of AFAIs, which is realized by combining the generalized-reflection-coefficient method and the T-matrix algorithm. Then, the three-dimensional (3-D) RCSs of the AFAIs can be approximately obtained from the 2-D radar scattering width according to Knott's equation [29]. The generalized-reflection-coefficient

Manuscript received 30 November 2022; revised 30 January 2023; accepted 28 February 2023. Date of publication 3 March 2023; date of current version 16 March 2023. This work was supported by the National Key Laboratory of Electromagnetic Environment under Grant 6142403200304. *(Corresponding author: Wei E. I. Sha.)*

Shuai S. A. Yuan and Wei E. I. Sha are with the College of Information Science and Electronic Engineering, Zhejiang University, Hangzhou 310027, China (e-mail: shuaiyuan1997@zju.edu.cn; weisha@zju.edu.cn).

Zhu Hong Lin is with the School of Information Science and Electronic Engineering, Hangzhou City University, Hangzhou 310015, China (e-mail: linzhuhong@zju.edu.cn).

Li-Bin Lv and Shu-Ji Hao are with the National Key Laboratory of Electromagnetic Environment, China Research Institute of Radiowave Propagation, Qingdao 266107, China (e-mail: libin_lv@163.com; hsj80586@yahoo.com.cn).

Digital Object Identifier 10.1109/JMMCT.2023.3252053

method is widely used for analytically solving the scattering problems of regular multilayer structures, the generalized reflection coefficients can be deduced based on the permittivities and boundary conditions of each layer [30]. The T-matrix method is a typical computational technique for solving many-body scattering problems [31], which can accurately describe the interactions between multiple scatterers [32], [33]. In various applications, it can compare favorably with other frequently-used computation methods in terms of accuracy, efficiency and parameter range [34], [35], [36], [37]. T-matrix method has been proved to be highly efficient and been widely implemented in computing electromagnetic scattering of single and compound scatterers.

In this paper, we start with the physical model of AFAIs, including the isotropic approximation of the ionospheric medium in the desired frequency band, the geometry of AFAIs, and the plasma cutoff frequency of AFAIs. Next, the generalized-reflection-coefficient method is used for deriving the expansion coefficients of the scattered field of a single AFAI under the cylindrical harmonic functions, which yields the entries of the T-matrix. Then, the T-matrix algorithm is used to establish the matrix equations for solving the scattered field of multiple AFAIs. The expansion coefficients of the total scattered field in the global coordinate system and the objective RCS are calculated. After that, the RCSs of one, two and 3×3 AFAIs under normal and oblique incidences (including TM and TE waves) are presented and compared to the results obtained from full-wave simulations. Moreover, the errors brought by the isotropic approximation are discussed in Appendix A, and the translational formulas for cylindrical harmonic functions are discussed in Appendix B. This paper proposes an analytical method for rapidly calculating the objective RCSs of AFAIs based on T-matrix algorithm, which can be applied to analyze and predict the performance of ionospheric AFAI-based long-wave communications.

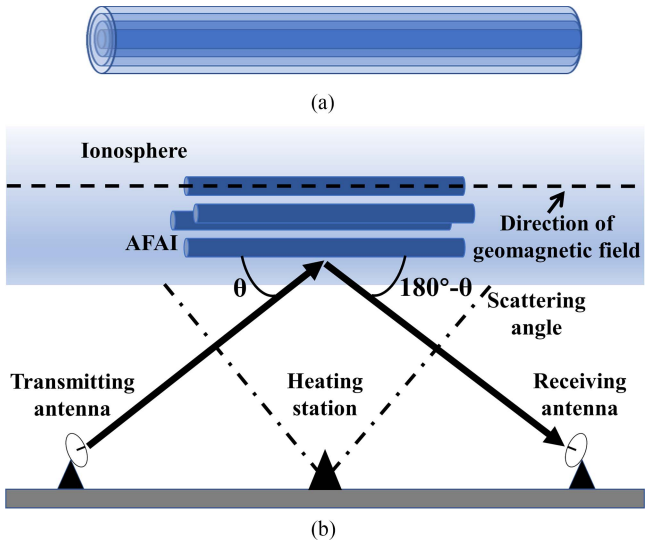

Fig. 1. Physical model of AFAIs. (a) Single AFAI. (b) Multiple AFAIs working as reflectors for long-wave communications.

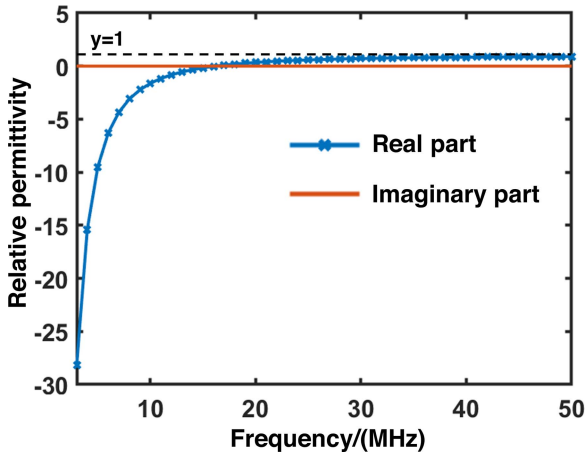

Fig. 2. Relative permittivities of the central layer of AFAI at different frequencies.

II. Physical Model of AFAIs

The geometry of a single AFAI can be approximated as an elongated multilayer cylinder with different electron densities in each layer, where the electron densities gradually decrease from the inside to the outside following a Gaussian distribution [25], [26], as shown in Fig. 1(a). The ionosphere is artificially heated for generating multiple AFAIs, the AFAIs can reflect relatively low frequency electromagnetic waves for realizing long-distance communications, as depicted in Fig. 1(b). The electromagnetic properties of AFAIs can be strictly described by the magnetized plasma model [38], and approximated by the Drude model at the desired frequency band in this paper [39], as discussed in Appendix A. Without loss of generality, a single AFAI is modeled as a 9-layer plasma cylindrical structure, with the radius $R = 55$ m and the length $H = 1100$ m. The outermost electron density of the AFAI is taken as 6.5×10^{11} (1/m^{-3}) according to the International Reference Ionosphere (IRI) model [40], and the electron density of the central layer is set to be 5 times the outermost electron density. The effect of background ionosphere is neglected in this paper, since its electron density is low compared to the AFAIs, and the electromagnetic waves at the interested frequencies will mostly pass through the background ionosphere.

The plasma cutoff frequency of each layer is presented in Table I (the first layer is the central layer). According to Appendix A, we can calculate the permittivities of the central layer at different frequencies, as demonstrated in Fig. 2. At relatively low frequencies, the real part of the permittivity is negative, hence, the AFAIs can produce strong scattered fields along the objective direction.

However, when the frequency becomes higher, the real part of the plasma permittivity tends to 1, and the incident field can mostly pass through the AFAIs. For ionospheric AFAI-based communications, it is crucial to quickly evaluate whether the AFAIs can produce a strong signal along the desired direction at a certain frequency. Due to the large electrical size of AFAIs, calculating RCSs by full-wave simulations is time-consuming and requires large computer memory. Considering the slender

TABLE I
CUTOFF ANGULAR FREQUENCIES OF THE EACH LAYER OF AFAI

Layer	1	2	3	4	5	6	7	8	9
Cutoff angular frequency($\times 10^6$ rad/s)	102	101	98	93	87	79	71	63	54

geometry of single AFAI, its scattering characteristic is similar to that of a 2-D multilayer cylinder. Therefore, we utilize analytical methods to calculate the radar scattering width of multiple multilayer infinitely-long cylinders with the same radii as AFAIs, then approximate the 3-D RCSs of the AFAIs from the radar scattering width based on Knott's equation. It should be noticed that the proposed analytical method could only work accurately under the following two conditions. First, the AFAIs can be approximated as elongated cylinders, or else the Knott's equation is inaccurate. Second, the AFAIs can be regarded as isotropic media at the interested frequencies, which should be carefully evaluated according to the physical parameters of the plasma.

III. METHODOLOGY

A. Scattering of Single AFAI

In this subsection, the generalized-reflection-coefficient method is used for analytically solving the scattering problem of a single infinitely-long AFAI [30]. To calculate the scattered field of a 2-D cylindrical structure, the incident plane wave should be expanded into multi-order cylindrical harmonic functions, and the generalized reflection coefficients of the cylindrical harmonic functions can be obtained according to the boundary conditions and the recursive relations.An incident plane wave propagating along any direction can be expanded in the cylindrical coordinate system as

$$\begin{aligned}\mathbf{E}^{inc}(\boldsymbol{\rho},z) &= e^{-jk_z z}\sum_{n=-\infty}^{\infty}\Re g\bar{\Psi}_n^t\left(k_\rho,\boldsymbol{\rho}-\boldsymbol{\rho}_0\right)\cdot\mathbf{a}_n^{inc}\\ &= e^{-jk_z z}\sum_{n=-\infty}^{\infty}a_n^{inc(M)}[\Re g\mathbf{M}_n\left(k_\rho,\boldsymbol{\rho}-\boldsymbol{\rho}_0\right)\\ &\quad + a_n^{inc(N)}\Re g\mathbf{N}_n\left(k_\rho,\boldsymbol{\rho}-\boldsymbol{\rho}_0\right)]\\ &= e^{-jk_z z}\sum_{n=-\infty}^{\infty}j^{-n}e^{jn\phi}[E_0J_n(k_\rho|\boldsymbol{\rho}-\boldsymbol{\rho}_0|)\\ &\quad + H_0J_n(k_\rho|\boldsymbol{\rho}-\boldsymbol{\rho}_0|)],\end{aligned}\tag{1}$$

where $\bar{\Psi}_n^t$ are the cylindrical harmonic functions (containing TM and TE waves), $\Re g$ represents the regular part of the cylindrical harmonic functions (from propagating waves to standing waves), $\mathbf{a}_n^{inc}$ are the expansion coefficients (containing the TM wave expansion coefficients $a_n^{inc(M)}$ and the TE wave expansion coefficients $a_n^{inc(N)}$, M and N indicate the expansion coefficients for TM and TE waves), $\mathbf{M}_n$ and $\mathbf{N}_n$ represent the cylindrical harmonic functions for TM and TE waves, respectively. The tangential components of both TM and TE waves can be expanded as a superposition of the cylindrical Bessel functions J_n, and their expansion coefficients differ by a factor of the wave impedance. Similarly, the scattered field can be expanded as

$$\begin{aligned}\mathbf{E}^{sca}(\boldsymbol{\rho},z) &= e^{-jk_z z}\sum_{n=-\infty}^{\infty}\bar{\Psi}_n^t\left(k_\rho,\boldsymbol{\rho}-\boldsymbol{\rho}_0\right)\cdot\mathbf{a}_n^{sca}\\ &= e^{-jk_z z}\sum_{n=-\infty}^{\infty}[a_n^{sca(M)}\mathbf{M}_n\left(k_\rho,\boldsymbol{\rho}-\boldsymbol{\rho}_0\right)\\ &\quad + a_n^{sca(N)}\mathbf{N}_n\left(k_\rho,\boldsymbol{\rho}-\boldsymbol{\rho}_0\right)]\\ &= e^{-jk_z z}\sum_{n=-\infty}^{\infty}[a_n^{sca(M)}H_n^{(2)}(k_\rho|\boldsymbol{\rho}-\boldsymbol{\rho}_0|)\\ &\quad + a_n^{sca(N)}H_n^{(2)}(k_\rho|\boldsymbol{\rho}-\boldsymbol{\rho}_0|)].\end{aligned}\tag{2}$$

The expansion coefficients of the incident and scattered fields can be related by the T matrix

$$\mathbf{a}^{sca}=\overline{\mathbf{T}}\cdot\mathbf{a}^{inc},\tag{3}$$

where $\mathbf{a}^{sca}=\begin{bmatrix}a^{sca(M)}\\ a^{sca(N)}\end{bmatrix}$, $\mathbf{a}^{inc}=\begin{bmatrix}a^{inc(M)}\\ a^{inc(N)}\end{bmatrix}$. The entries of the T matrix are

$$\overline{\mathbf{T}}=\begin{bmatrix}\overline{\mathbf{T}}^{(11)} & \overline{\mathbf{T}}^{(12)}\\ \overline{\mathbf{T}}^{(21)} & \overline{\mathbf{T}}^{(22)}\end{bmatrix},\tag{4}$$

where each submatrix is a diagonal array, i.e., each order of the Bessel function J_n only generates the Hankel function $H_n^{(2)}$ of the corresponding order, and the submatrix can be written as

$$\begin{aligned}\overline{\mathbf{T}}_{nn'}^{(11)} &= \delta_{nn'}T_n^{(MM)}\\ \overline{\mathbf{T}}_{nn'}^{(12)} &= \delta_{nn'}T_n^{(MN)}\\ \overline{\mathbf{T}}_{nn'}^{(21)} &= \delta_{nn'}T_n^{(NM)}\\ \overline{\mathbf{T}}_{nn'}^{(22)} &= \delta_{nn'}T_n^{(NN)},\end{aligned}\tag{5}$$

where T_n can be analytically derived based on the boundary conditions. For a single-layer cylinder (region 1 represents medium and region 2 represents air), we can build the matrix

$$\begin{aligned}&\overline{\mathbf{B}}_n\left(k_{i\rho}\rho\right)=\\ &\frac{1}{k_{i\rho}^2\rho}\begin{bmatrix}-j\omega\epsilon_i k_{i\rho}\rho B_n'\left(k_{i\rho}\rho\right) & -nk_z B_n\left(k_{i\rho}\rho\right)\\ -nk_z B_n\left(k_{i\rho}\rho\right) & j\omega\mu_i k_{i\rho}\rho B_n'\left(k_{i\rho}\rho\right)\end{bmatrix},\end{aligned}\tag{6}$$

where $i=1,2$ represent the medium and air region, $k_{i\rho}$ represents the tangential component of the wavenumber in the ith layer, k_z represents the vertical component of the wavenumber. $\overline{\mathbf{B}}_n$ is $\overline{\mathbf{H}}_n^{(2)}$ or $\overline{\mathbf{J}}_n$, depending on whether B_n is defined to be $H_n^{(2)}$ or J_n. Based on the boundary conditions at the boundary

$\rho = a$, the reflection coefficient matrix can be written as

$$\begin{aligned}\overline{\mathbf{R}}_{21} &= \begin{bmatrix} T_n^{(MM)} & T_n^{(MN)} \\ T_n^{(NM)} & T_n^{(NN)} \end{bmatrix} \\ &= \overline{\mathbf{D}}^{-1} \cdot \left[J_n\left(k_{1\rho}a\right) \overline{\mathbf{J}}_n\left(k_{2\rho}a\right) - J_n\left(k_{2\rho}a\right) \overline{\mathbf{J}}_n\left(k_{1\rho}a\right) \right], \end{aligned} \tag{7}$$

the transmission coefficient matrix is

$$\overline{\mathfrak{T}}_{21} = \frac{2\omega}{\pi k_{2\rho}^2 a} \overline{\mathbf{D}}^{-1} \cdot \begin{bmatrix} \epsilon_2 & 0 \\ 0 & -\mu_2 \end{bmatrix}, \tag{8}$$

where

$$\overline{\mathbf{D}} = \left[\overline{\mathbf{J}}_n\left(k_{1\rho}a\right) H_n^{(2)}\left(k_{2\rho}a\right) - \overline{\mathbf{H}}_n^{(2)}\left(k_{2\rho}a\right) J_n\left(k_{1\rho}a\right) \right]. \tag{9}$$

The reflection coefficient matrix $\overline{\mathbf{R}}_{12}$ and transmission coefficient matrix $\overline{\mathfrak{T}}_{12}$ (the wave propagates from inside to outside) can be obtained with a similar method. When the plane wave is perpendicular to the cylinder, k_z is zero, i.e., $T_n^{(MN)}$ and $T_n^{(NM)}$ are zero, and there is no coupling between TE and TM waves. For a single multilayer cylinder ($1, 2 \cdots n$ represents layer 1 to layer n, and layer n is air), we can derive the generalized reflection coefficient matrix based on the boundary conditions

$$\begin{aligned}\tilde{\overline{\mathbf{R}}}_{i,i-1} = \overline{\mathbf{R}}_{i,i-1} + \overline{\mathfrak{T}}_{i-1,i} \cdot \tilde{\overline{\mathbf{R}}}_{i-1,i-2} \cdot \\ \left(\overline{\mathbf{I}} - \overline{\mathbf{R}}_{i-1,i} \cdot \tilde{\overline{\mathbf{R}}}_{i-1,i-2} \right)^{-1} \cdot \overline{\mathfrak{T}}_{i,i-1}, \end{aligned} \tag{10}$$

where $\tilde{\overline{\mathbf{R}}}_{i,i-1}$ is the generalized reflection coefficient matrix from the ith to the $(i-1)$th layer (including the internal multiple reflections), $\overline{\mathbf{R}}_{i,i-1}$ is the reflection coefficient matrix from the ith to the $(i-1)$th layer, $\overline{\mathfrak{T}}_{i,i-1}$ is the transmission coefficient matrix from the ith to the $(i-1)$th layer. Therefore, starting from the innermost layer ($\tilde{\overline{\mathbf{R}}}_{1,0} = 0$), we can iteratively solve the outermost generalized scattering coefficient matrix $\tilde{\overline{\mathbf{R}}}_{i,i-1}$, so as to get the element values in $\overline{\mathbf{T}}$ matrix.

B. Scattering of Multiple AFAIs

Assuming there are P_n AFAIs, the total scattered field can be written as

$$\mathbf{E}^{sca}(\boldsymbol{\rho}, z) = \sum_{i=1}^{P_n} \mathbf{E}_i^{sca}(\boldsymbol{\rho}, z), \tag{11}$$

where $\mathbf{E}_i^{sca}(\boldsymbol{\rho}, z)$ is the scattered field of the ith scatterer, and $\mathbf{E}_i^{sca}(\boldsymbol{\rho}, z)$ can be expanded as

$$\mathbf{E}_i^{sca}(\boldsymbol{\rho}, z) = \sum_n \bar{\Psi}_n^t\left(k_\rho, \boldsymbol{\rho} - \boldsymbol{\rho}_i\right) \cdot \mathbf{a}_n^i, \tag{12}$$

where $\boldsymbol{\rho}_i$ is the center of the ith scatterer. Since the coefficients are obtained by expanding the scattered field of each scatterer at its local coordinate center, the coordinate translation $\boldsymbol{\rho} - \boldsymbol{\rho}_i$ here represents the translation of the field centered at each scatterer to the field centered at the global coordinate center. Different scatterers are expanded at different coordinate centers, and the coordinate translational formulas are

$$\begin{aligned}\overline{\boldsymbol{\Psi}}_n^t(k, \boldsymbol{\rho}) = \sum_{n'} \Re g \overline{\boldsymbol{\Psi}}_{n'}^t\left(k, \boldsymbol{\rho}'\right) \cdot \overline{\boldsymbol{\alpha}}_{n',n}\left(\boldsymbol{\rho} - \boldsymbol{\rho}'\right), \\ \left|\boldsymbol{\rho}'\right| < \left|\boldsymbol{\rho} - \boldsymbol{\rho}'\right|, \end{aligned} \tag{13}$$

$$\begin{aligned}\overline{\boldsymbol{\Psi}}_n^t(k, \boldsymbol{\rho}) = \sum_{n'} \overline{\boldsymbol{\Psi}}_{n'}^t\left(k, \boldsymbol{\rho}'\right) \cdot \overline{\boldsymbol{\beta}}_{n',n}\left(\boldsymbol{\rho} - \boldsymbol{\rho}'\right), \\ \left|\boldsymbol{\rho}'\right| > \left|\boldsymbol{\rho} - \boldsymbol{\rho}'\right|, \end{aligned} \tag{14}$$

$$\begin{aligned}\Re g \overline{\boldsymbol{\Psi}}_n^t(k, \boldsymbol{\rho}) = \sum_{n'} \Re g \overline{\boldsymbol{\Psi}}_{n'}^t\left(k, \boldsymbol{\rho}'\right) \cdot \overline{\boldsymbol{\beta}}_{n',n}\left(\boldsymbol{\rho} - \boldsymbol{\rho}'\right), \\ \forall \left|\boldsymbol{\rho}'\right|, |\boldsymbol{\rho}|. \end{aligned} \tag{15}$$

For the ith cylinder, at its coordinate center, the incident wave are the outward wave emitted from the excitation source plus the outward waves scattered from all other cylinders

$$\begin{aligned}\mathbf{E}_i^{inc}(\boldsymbol{\rho}, z) &= \mathbf{E}^{inc}(\boldsymbol{\rho}, z) + \sum_{j \neq i} \mathbf{E}_j^{sca}(\boldsymbol{\rho}, z) \\ &= \sum_n \bar{\Psi}_n^t(k, \boldsymbol{\rho} - \tilde{\boldsymbol{\rho}}) \cdot \mathbf{b}_n + \sum_{j \neq i} \sum_n \bar{\Psi}_n^t(k, \boldsymbol{\rho} - \boldsymbol{\rho}_j) \cdot \mathbf{a}_n^j, \end{aligned} \tag{16}$$

where $\tilde{\boldsymbol{\rho}}$ is the reference coordinate center of the source, and all outward waves are converted to inward waves after bringing in the translational formulas

$$\begin{aligned}\mathbf{E}_i^{inc}(\boldsymbol{\rho}, z) &= \sum_n \Re g \overline{\boldsymbol{\Psi}}_n^t\left(k, \boldsymbol{\rho} - \boldsymbol{\rho}_i\right) \sum_{n'} \overline{\boldsymbol{\alpha}}_{n,n'}\left(\boldsymbol{\rho}_i - \tilde{\boldsymbol{\rho}}\right) \cdot \mathbf{b}_{n'} \\ &\quad + \sum_{j \neq i} \sum_n \Re g \overline{\boldsymbol{\Psi}}_n^t\left(k, \boldsymbol{\rho} - \boldsymbol{\rho}_i\right) \sum_{n'} \overline{\boldsymbol{\alpha}}_{n,n'}(\boldsymbol{\rho}_i - \boldsymbol{\rho}_j) \cdot \mathbf{a}_{n'}^j \\ &= \sum_n \Re g \overline{\boldsymbol{\Psi}}_n^t\left(k, \boldsymbol{\rho} - \boldsymbol{\rho}_i\right) \left[\sum_{n'} \overline{\boldsymbol{\alpha}}_{n,n'}\left(\boldsymbol{\rho}_i - \tilde{\boldsymbol{\rho}}\right) \right. \\ &\quad \left. \cdot \mathbf{b}_{n'} + \sum_{j \neq i} \sum_{n'} \overline{\boldsymbol{\alpha}}_{n,n'}\left(\boldsymbol{\rho}_i - \boldsymbol{\rho}_j\right) \cdot \mathbf{a}_{n'}^j \right]. \end{aligned} \tag{17}$$

If the source is a plane wave and the reference center is the global coordinate center, we extract the $e^{-jk_z z}$ component to derive the expansion coefficients of the tangential component of the incident field for the ith cylinder as

$$\mathbf{h}_n^i = \left[\mathbf{b}_n^i + \sum_{j \neq i} \sum_{n'} \overline{\boldsymbol{\alpha}}_{n,n'}\left(\boldsymbol{\rho}_i - \boldsymbol{\rho}_j\right) \cdot \mathbf{a}_{n'}^j \right], \tag{18}$$

$\mathbf{b}_n^i$ represents the expansion coefficients of the tangential component of the incident plane wave when the ith scatterer is regarded as the coordinate center. For TM waves, the expansion coefficients are

$$b_n = j^{-n} e^{-j(k_x x_i + k_y y_i)} e^{jn\phi}, \tag{19}$$

based on the T matrix of a single AFAI, we can obtain

$$\mathbf{a}^i = \overline{\mathbf{T}}^i \cdot \mathbf{h}^i, \quad i = 1, \ldots, P_n, \tag{20}$$

where $\mathbf{a}^i$ are the expansion coefficients of the scattered field of the ith cylinder (to be solved), and $\overline{\mathbf{T}}^i$ is the T matrix of the ith cylinder. A number of P_n matrices can form a matrix equation, where the expansion coefficients of the scattered fields of each cylinder are the unknowns. We write all the expansion coefficients into a vector, and (18) can be written as the matrix equation

$$\overline{\mathbf{a}} = \overline{\overline{\mathbf{T}}} \cdot \left[\overline{\mathbf{b}} + \overline{\overline{\mathbf{A}}} \cdot \overline{\mathbf{a}}\right], \tag{21}$$

where $\overline{\overline{\mathbf{A}}}$ is the operator that takes into account the central coordinate shift and the summation of the scattered fields of the other j scatterers in (18). (21) can be solved by the inverse of matrix

$$\overline{\mathbf{a}} = \left(\overline{\overline{\mathbf{I}}} - \overline{\overline{\mathbf{T}}}\,\overline{\overline{\mathbf{A}}}\right)^{-1} \overline{\overline{\mathbf{T}}} \cdot \overline{\mathbf{b}}, \tag{22}$$

the specific elements of the matrix are presented in (23) shown at the bottom of this page.

In (23), assume there are $n = (2M+1)$ cylindrical harmonic functions. Then, $\mathbf{a}^i$ and $\mathbf{b}^i$ are $2(2M+1) \times 1$ column vectors, representing the expansion coefficient of the scattered field and the incident plane wave (including TM and TE polarizations) when the ith scatterer is the coordinate center. $\overline{\mathbf{T}}^i$ is a $2(2M+1) \times 2(2M+1)$ matrix, representing the T matrix between the incident field and the scattered field for each scatterer. $\mathbf{0}$ represents the matrix where all the elements are 0. The $\boldsymbol{\alpha}_{i,j}$ with dimension $2(2\,M+1) \times 2(2M+1)$ represents the transition matrix from the jth scatterer to the ith scatterer, including the TM and TE waves, as discussed in Appendix B. The matrix form of $\boldsymbol{\alpha}_{i,j}$ is

$$\boldsymbol{\alpha}_{i,j} = \begin{bmatrix} \boldsymbol{\alpha}_{i,j}^M & \mathbf{0} \\ \mathbf{0} & \boldsymbol{\alpha}_{i,j}^N \end{bmatrix}, \tag{24}$$

where $\boldsymbol{\alpha}_{i,j}^M$ represents the transition matrix for TM waves, and $\boldsymbol{\alpha}_{i,j}^N$ represents the transition matrix for TE waves, their matrix dimensions are both $(2M+1) \times (2M+1)$.

C. Formulas of RCS

Based on the above equations, the expansion coefficients of the scattered fields of single and multiple 2-D AFAIs are solved. Then, we can approximately calculate the objective RCSs of 3-D AFAIs. When the incident plane wave is along the θ direction, the radar scattering width of the 2-D cylinder along the $180^\circ - \theta$ direction (objective RCS direction) can be calculated with [41]

$$\sigma_{2\mathrm{D}} = \lim_{\rho\to\infty} \frac{2\pi\rho}{\sin\theta} \frac{|E_z^{\mathrm{sc}}|^2 + |Z_0 H_z^{\mathrm{sc}}|^2}{|E_z^{\mathrm{inc}}|^2 + |Z_0 H_z^{\mathrm{inc}}|^2}, \tag{25}$$

where θ is the incident angle, $|E_z^{\mathrm{sc}}|$ and $|Z_0 H_z^{\mathrm{sc}}|$ are the scattered fields of TM and TE waves, and Z_0 is the free-space wave impedance. Since the scattered field can be expanded under $H_n^{(2)}$, after solving for the expansion coefficients of the total scattered field, we can use the far-field form of $H_n^{(2)}$ to obtain the scattering width. When ρ tends to infinity, we have [30]

$$H_n^{(2)}(k_\rho \rho) \sim \sqrt{\frac{2}{\pi k_\rho \rho}} e^{-j\left(k_\rho \rho - \frac{n\pi}{2} - \frac{\pi}{4}\right)}. \tag{26}$$

Combining Eqs. (25) and (26), the distance term ρ is eliminated, while $k_\rho \rho$ and $-\frac{\pi}{4}$ in the exponential term do not affect the results. If the amplitude of E_z^{inc} is 1 and the amplitude of H_z^{inc} is $1/Z_0$, the expression for radar scattering width would be

$$\sigma_{2\mathrm{D}} = \frac{2}{k_\rho \sin\theta} \left[\left| \sum_{n=-\infty}^{\infty} a_n^M \exp(jn\pi/2 + jn\phi) \right|^2 + \left| \sum_{n=-\infty}^{\infty} Z_0 a_n^N \exp(jn\pi/2 + jn\phi) \right|^2 \right], \tag{27}$$

where a_n^M and a_n^N represent the expansion coefficients of TM and TE waves. In fact, the $\exp(jn\pi/2 + jn\phi)$ is used as the expansion base instead of the Hankel function when calculating the far-field RCS. After obtaining the 2D scattering width, we can approximate the 3-D RCS of according to Knott's equation [29]

$$\sigma_{3D} = (2\sigma_{2D}/\lambda_0) \left| \frac{H \sin(k_0 H \cos(\theta))}{k_0 H \cos(\theta)} \right|^2, \tag{28}$$

where H is the length of the cylinder and k_0 is the free-space wavenumber. This equation assumes that there are no reflections at the upper and lower edges inside the cylinders, so it is suitable for slender cylindrical structures such as AFAIs. The errors brought by using (28) will become larger at oblique incidence compared to perpendicular incidence, due to the stronger reflections at the edges inside the cylinders. Although there are errors by implementing this approximate method for estimating the 3-D RCS of AFAIs, the errors in the objective scenario are acceptable, as we discussed in the next section.

IV. Numerical Results

A. RCS of AFAI

In this subsection, we present the RCSs of one, two and 3×3 AFAIs under the incidences of both TM and TE waves. For the parameters of the AFAI, the single AFAI is modeled as a nine-layer plasma cylindrical structure with length $H = 1100$ m and radius $R = 55$ m, and each layer has the same thickness. The cutoff frequencies of the plasmas in the nine layers are the same

$$\begin{bmatrix} \mathbf{a}^1 \\ \mathbf{a}^2 \\ \vdots \\ \mathbf{a}^{P_n} \end{bmatrix} = \begin{bmatrix} \overline{\mathbf{T}}^1 & \mathbf{0} & \cdots & \mathbf{0} \\ \mathbf{0} & \overline{\mathbf{T}}^2 & \cdots & \mathbf{0} \\ \vdots & \vdots & \ddots & \vdots \\ \mathbf{0} & \mathbf{0} & \cdots & \overline{\mathbf{T}}^{P_n} \end{bmatrix} \cdot \left(\begin{bmatrix} \mathbf{b}^1 \\ \mathbf{b}^2 \\ \vdots \\ \mathbf{b}^{P_n} \end{bmatrix} + \begin{bmatrix} \mathbf{0} & \boldsymbol{\alpha}_{1,2} & \cdots & \boldsymbol{\alpha}_{1,P_n} \\ \boldsymbol{\alpha}_{2,1} & \mathbf{0} & \cdots & \boldsymbol{\alpha}_{2,P_n} \\ \vdots & \vdots & \ddots & \vdots \\ \boldsymbol{\alpha}_{P_n,1} & \boldsymbol{\alpha}_{P_n,2} & \cdots & \mathbf{0} \end{bmatrix} \cdot \begin{bmatrix} \mathbf{a}^1 \\ \mathbf{a}^2 \\ \vdots \\ \mathbf{a}^{P_n} \end{bmatrix} \right) \tag{23}$$

TABLE II
RELATIVE ERRORS OF THE RCSS OF AFAIS CALCULATED WITH ANALYTICAL METHOD UNDER OBLIQUE INCIDENCE

No. of AFAIs	TM wave			TE wave		
	Single	Double	3×3	Single	Double	3×3
Relative error	3 %	0.7 %	4 %	1 %	0.5 %	2.5 %

TABLE III
COMPUTATIONAL COSTS OF THE RCSS OF AFAIS UNDER OBLIQUE INCIDENCE (NUMERICAL/ANALYTICAL)

No. of AFAIs	TM wave			TE wave		
	Single	Double	3×3	Single	Double	3×3
Memory	28 G/2.54 G	50 G/2.55 G	210 G /2.6 G	33 G/2.54 G	51G /2.55 G	232 G/2.6 G
Time	0.5 h/0.57 s	2.2 h/0.66 s	7.9 h/3.85 s	0.8 h/0.57 s	2.3 h/0.66 s	8.8 h/3.85 s

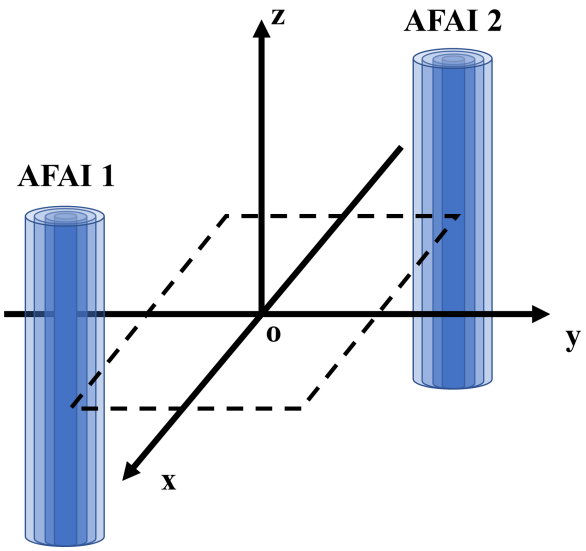

Fig. 3. Positions of the two AFAIs in Cartesian coordinate.

as that in Table I. When calculating the scattered field of a single AFAI, the geometric center of AFAI is located at the global coordinate center. In the case of the two AFAIs shown in Fig. 3, the coordinate positions are $(-3R, -3R)$ and $(3R, 3R)$, with the height of cylinder ranging from $-H/2$ to $H/2$. When calculating the scattered field of 3×3 AFAIs, the x and y coordinates are taken as the values within $[-3R, 0, 3R]$, i.e., the cylinders are uniformly distributed with a spacing of $3R$. The wavelength of the incident plane wave is set as 55 m (5.45 MHz), and two representative angles are taken as the incident angles, including the perpendicular incidence ($\theta = 90°, \phi = 180°$) for monostatic RCS and the oblique incidence ($\theta = 135°, \phi = 180°$) for bistatic RCS.

The RCSs are calculated based on the T-matrix algorithm in Section III, and then compared to the results obtained from full-wave simulations empowered by commercial software CST MWS. When the incident plane wave is perpendicular to the cylinders ($\theta = 90°, \phi = 180°$), the comparisons of the RCSs are shown in Fig. 4. In perpendicular incidences, the results obtained from the T-matrix algorithm are almost the same as that obtained from full-wave simulations, proving the validity of the generalized-reflection-coefficient method and the T-matrix algorithm. Under the oblique incidence ($\theta = 135°, \phi = 180°$), the comparisons of the RCSs are shown in Fig. 5. The errors brought by (28) become larger in some scenarios, because the reflections at the ends of the cylinders are stronger. Therefore, we can find that the errors are more obvious at some ϕ angles, such as $\phi = 0°$ in Fig. 5(a), $\phi = 30°$ in Fig. 5(b) and $\phi = 60°$ in Fig. 5(e). However, as presented in Table II, the relative errors of RCSs along the objective direction of $\theta = 45°, \phi = 180°$ are less than 5%, which is generally acceptable for estimating the performance of AFAI-based long-wave communications. Meanwhile, compared to full-wave simulations, the computation time can be reduced from several hours to several seconds by applying the analytical T-matrix algorithm. The specific computational costs (memory and time) with numerical and analytical methods are compared in Table III, it can be found that the computational costs are significantly reduced by applying the T-matrix algorithm, and more calculation time is needed when the number of AFAIs increases.

TABLE IV
RCSS OF ONE AFAI AT DIFFERENT FREQUENCIES

	TM wave		TE wave	
	Analytical	Numerical	Analytical	Numerical
5 MHz	65.76	67.31	70.19	69.35
8 MHz	63.62	65.24	65.69	66.07
15 MHz	54.18	56.50	54.12	56.55

TABLE V
RCSS OF 3×3 AFAIS AT DIFFERENT FREQUENCIES

	TM wave		TE wave	
	Analytical	Numerical	Analytical	Numerical
5 MHz	84.83	82.28	85.66	84.23
8 MHz	81.74	78.61	76.03	79.25
15 MHz	66.90	68.22	58.84	62.57

B. *Objective RCSs At Different Frequencies*

The electrical sizes of AFAIs are large at high frequencies, thus it is time-consuming to calculate the RCSs by full-wave simulations. We compare the objective RCSs ($\theta = 45°, \phi = 180°$) of one and 3×3 AFAIs at 5 MHz, 8 MHz and 15 MHz under oblique incidence ($\theta = 135°, \phi = 180°$), as presented in Table IV and Table V. When calculating the objective RCS of a single AFAI, the results obtained from T-matrix algorithm are in good agreement with the results obtained from full-wave simulations, where the relative errors are within %5. For 3×3

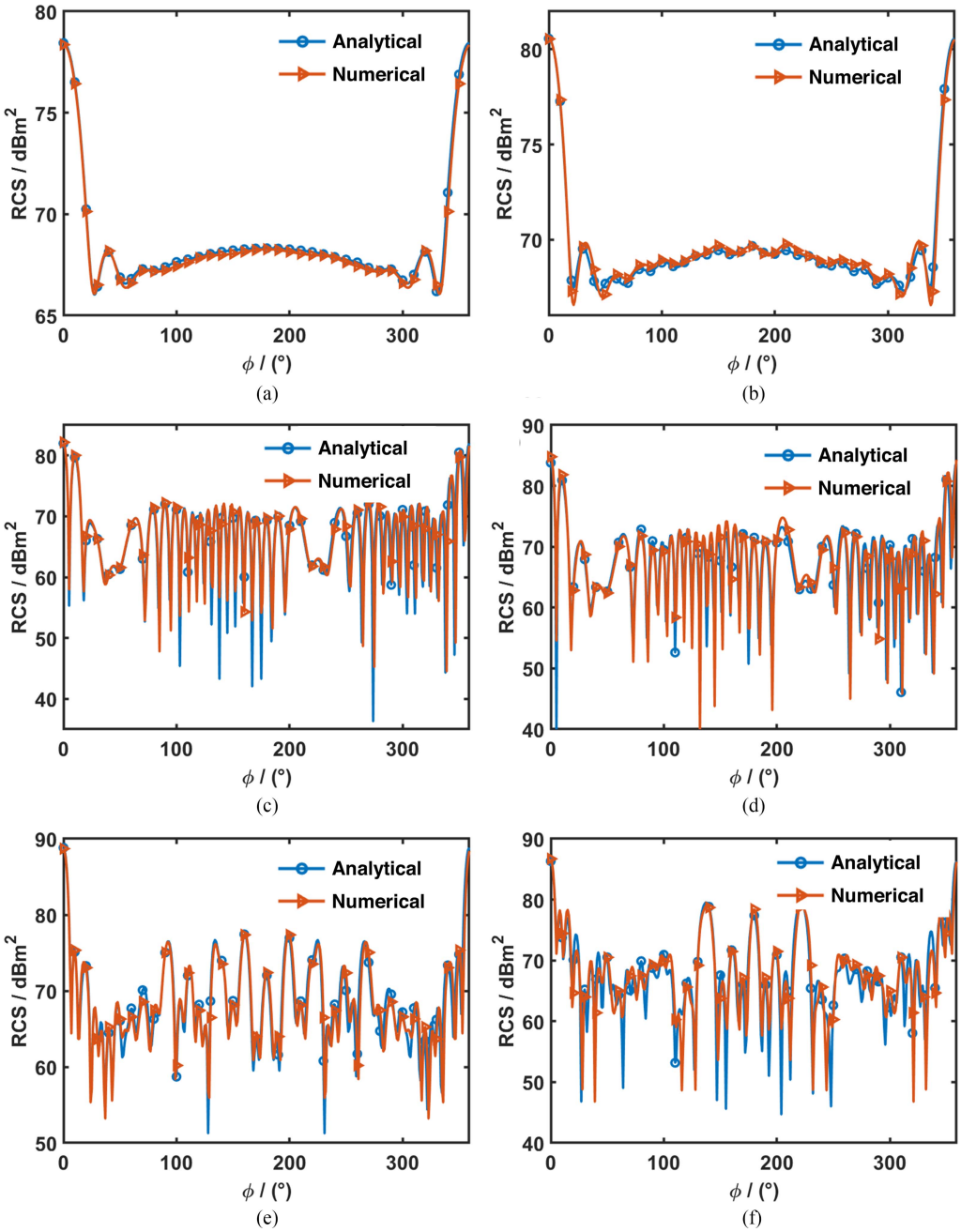

Fig. 4. RCSs ($\theta = 90°, \phi = 0° - 359°$) of AFAIs under the incidences of TM and TE waves (incident angle: $\theta = 90°, \phi = 180°$). (a-b) RCSs of one AFAI under the incidences of TM and TE waves. (c-d) RCSs of two AFAIs under the incidences of TM and TE waves. (e-f) RCSs of 3×3 AFAIs under the incidences of TM and TE waves.

AFAIs, the RCS errors are relatively large (3.73 dB) under the incidence of 15 MHz TE wave, but the relative errors in the other cases are all within $\%5$.

Furthermore, based on the T-matrix algorithm, we calculate the objective RCSs ($\theta = 45°, \phi = 180°$) of one and 3×3 AFAIs under oblique incidence ($\theta = 135°, \phi = 180°$) at different frequencies, as shown in Fig. 6. Within the frequency range of 5–50 MHz, the objective RCSs of AFAIs gradually decreases, which is in consistent with the results indicated by Fig. 2. Also, larger number of AFAIs can produce larger RCS, and the RCS becomes oscillating at some frequencies. Considering the parameters of AFAIs set in this paper, the performance of AFAI-based communication is relatively good within the frequency range 5-15 MHz, where the decrease of RCS from 5 MHz to 15 MHz is smaller than 20 dBm^2. When the frequency becomes higher than 50 MHz, the signals will almost pass through the AFAIs. This paper verifies the applicability of estimating the objective RCS by the T-matrix algorithm, and the specific parameters of AFAIs can be set according to the practical requirements.

In addition, from Tables IV and V, it can be found that the analytical method is more accurate at relatively low frequencies,

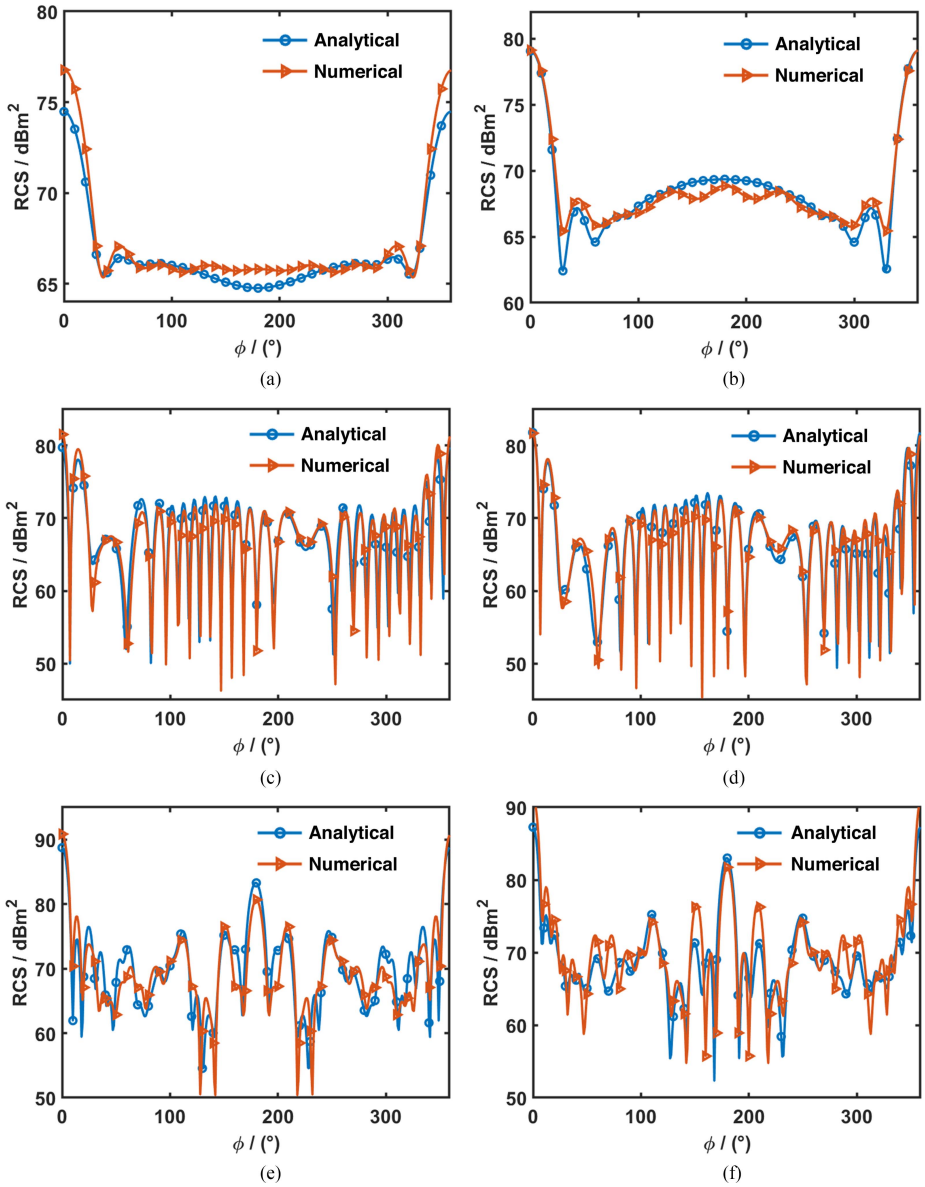

Fig. 5. RCSs ($\theta = 45°, \phi = 0° - 359°$) of AFAIs under the incidences of TM and TE waves (incident angle: $\theta = 135°, \phi = 180°$). (a)–(b) RCSs of one AFAI under the incidences of TM and TE waves. (c)–(d) RCSs of two AFAIs under the incidences of TM and TE waves. (e)–(f) RCSs of 3×3 AFAIs under the incidences of TM and TE waves.

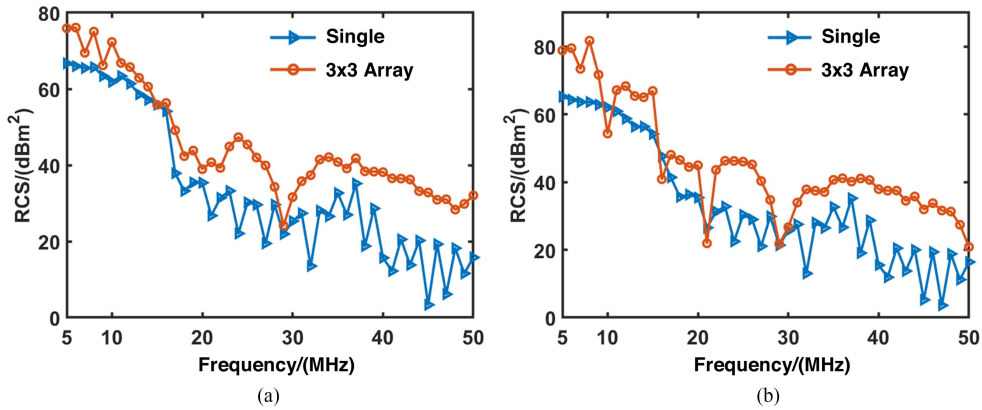

Fig. 6. Objective RCSs of AFAIs at different frequencies. (a) TM wave. (b) TE wave.

i.e., the electrical sizes of AFAIs are not too large. At high frequencies, the analytical method requires a large number of cylindrical harmonic functions to maintain the accuracy of the solution. Meanwhile, the values of the cylindrical harmonic functions tend to be infinite or infinitesimal when the order of the cylindrical harmonic functions is too large, and the accuracy of the transition matrix is also difficult to be maintained at this time (translation of higher order cylindrical harmonic functions requires more expansion terms).

V. Conclusion

In this paper, based on the physical properties of AFAIs, T-matrix algorithm is used for analytically estimating the objective RCSs of AFAIs after making reasonable approximations. Compared to full-wave simulations, utilizing the T-matrix algorithm can reduce the computation time from several hours to several seconds, while maintaining the acceptable RCS errors. The scattering characteristics of AFAIs at different frequencies are investigated, indicating that AFAIs can only work as reflectors at relatively low frequencies (dependent on the specific parameters of AFAIs). The proposed method can be used for quickly predicting the performance of ionospheric AFAI-based communications.

Appendix A
Isotropic Approximation of AFAI

Within the frequency range considered in this paper, the anisotropic plasma in AFAIs can be degenerated into the isotropic plasma described by Drude model [39]. Although this approximation is not strict, the errors of objective RCSs brought by the isotropic approximation are within an acceptable range. The isotropic approximation can alleviate the computational burden, especially for the large-scale scattering problems in ionosphere.

According to magnetized plasma model [38], the permittivity of plasma in the ionosphere is a tensor

$$\hat{\epsilon} = \epsilon_0(\mathbf{I} + \mathbf{M}), \tag{29}$$

where ϵ_0 is the permittivity in free space, $\mathbf{I}$ is the identity matrix, and $\mathbf{M}$ is the electric polarization matrix of the ionosphere. The expression of the $\mathbf{M}$ matrix is

$$\mathbf{M} = -\frac{X}{U\left(U^2 - Y^2\right)} \begin{bmatrix} U^2 & -jUY & 0 \\ jUY & U^2 & 0 \\ 0 & 0 & U^2 - Y^2 \end{bmatrix}, \tag{30}$$

where $U = 1 - j\nu/\omega$, ν is the effective collision frequency of the ionosphere, $X = \omega_0^2/\omega^2$, $Y = \omega_H/\omega$, ω_0 is the plasma cutoff frequency of the ionosphere ($\omega_0^2 = \frac{N_e^2}{\epsilon_0 m_e}$), $\omega = 2\pi f$ is the angular frequency of incident wave, N_e is the electron density, m_e is the electron mass. ω_H is the electron cyclotron frequency of the ionosphere ($\omega_H = |\frac{eB_0}{m_e}|$, e is the electron charge), the specific parameters can be obtained from the International Reference Ionosphere Model (IRI) [40]. The magnetic induction density of the geomagnetic field B_0 generally ranges from 0.25 to 0.65 Gauss. When B_0 is 0.5 Gauss, $\omega_H \sim 8.8 \times 10^6$, and $\nu \sim 10^3$ is taken in this paper. Hence, the permittivity can be rewritten as

$$\widehat{\epsilon} = \epsilon_0 \begin{bmatrix} \epsilon_1 & j\epsilon_2 & 0 \\ -j\epsilon_2 & \epsilon_1 & 0 \\ 0 & 0 & \epsilon_3 \end{bmatrix}, \tag{31}$$

where

$$\begin{aligned} \epsilon_1 &= 1 - \frac{XU}{(U^2 - Y^2)} \\ \epsilon_2 &= \frac{XY}{(U^2 - Y^2)} \\ \epsilon_3 &= 1 - \frac{X}{U}. \end{aligned} \tag{32}$$

In the desired frequency band, $\nu/\omega \ll 1$, i.e., $U \approx 1$. if U^2 is large compared to Y^2, then $\epsilon_1 \approx \epsilon_3$, $\epsilon_2 \approx 0$, and the anisotropic plasma degenerates to the isotropic medium. When the frequency of incident wave is 5 MHz, $Y^2 = (\omega_H/\omega^2) = 0.078$, which is small compared to U^2. The specific values of $\epsilon 2/\epsilon 1$ and $\epsilon 3/\epsilon 1$ at different frequencies are shown in Fig. 7, it can be found that ϵ_3 is very close to ϵ_1 and the value of ϵ_2/ϵ_1 is small when the frequency is larger than 5 MHz. To further analyze the specific effects of isotropic approximation, we calculate the objective RCSs of anisotropic and isotropic cylinders under different incident angles by full-wave simulations. The cylinder size and electron density are consistent with the numerical examples in Fig. 4(a)–(b), and the results are depicted in Fig. 8. Considering the AFAIs investigated in this paper, we can find that the isotropic approximation brings acceptable relative errors (within 5%) on objective RCSs when the frequency is higher than 5 MHz.

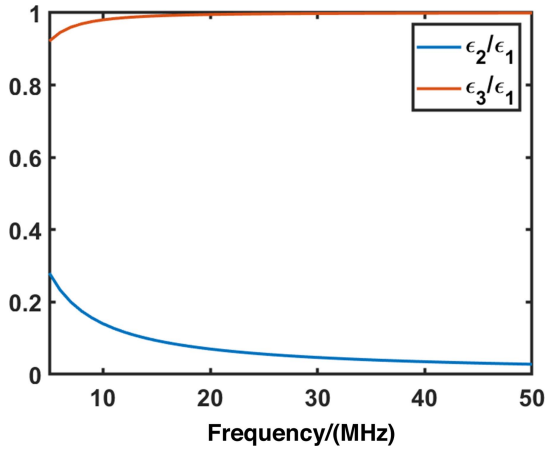

Fig. 7. The values of $\epsilon 2/\epsilon 1$ and $\epsilon 3/\epsilon 1$ at different frequencies.

Appendix B
Translational Formula

The translational formula of Hankel function is [30]

$$H_m^{(2)}\left(k_\rho\left|\rho - \rho'\right|\right) e^{-jm\phi''} = \begin{cases} \sum_{n=-\infty}^{\infty} J_{n-m}\left(k_\rho\rho'\right) H_n^{(2)}\left(k_\rho\rho\right) e^{-jn\phi + j(n-m)\phi'}, & \rho > \rho' \\ \sum_{n=-\infty}^{\infty} H_{n-m}^{(2)}\left(k_\rho\rho'\right) J_n\left(k_\rho\rho\right) e^{-jn\phi + j(n-m)\phi'}, & \rho < \rho' \end{cases} \tag{33}$$

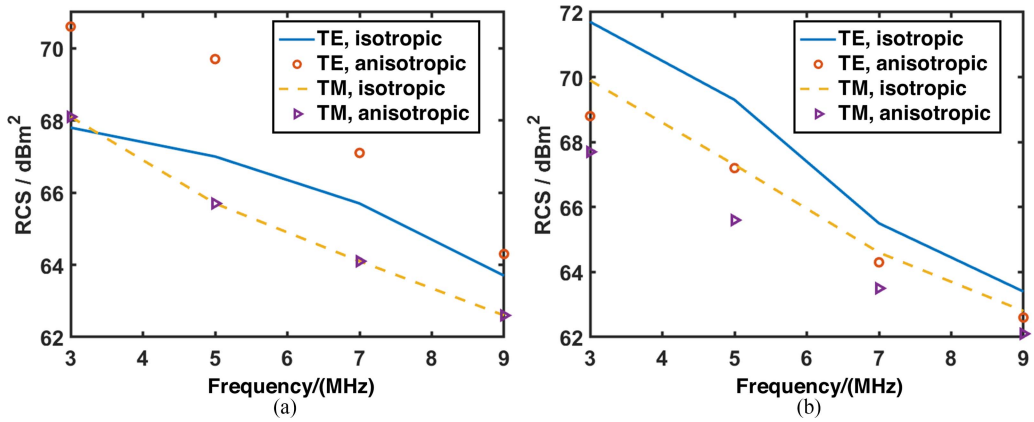

Fig. 8 The objective RCSs of isotropic and anisotropic cylinders at different frequencies and incident angles. (a) Perpendicular incidence ($\theta = 90°, \phi = 180°$), observation angle is $\theta = 90°, \phi = 180°$. (b) Oblique incidence ($\theta = 135°, \phi = 180°$), observation angle is $\theta = 45°, \phi = 180°$.

From the perspective of one scatterer, the scattered fields of the other scatterers are inward waves, so the translational formula used in this paper is the case of $\rho < \rho'$. The specific elements in the transition matrix are

$$[\boldsymbol{\alpha}_{ij}]_{nm} = H^{(2)}_{n-m}\left(k_\rho \phi'\right) e^{j(n-m)\phi'_{ij}}. \tag{34}$$

The number of the expansion coefficients of the translational formula is taken the same as that of the scattered field [35], which makes $\boldsymbol{\alpha}_{ij}$ a square matrix, otherwise the (23) cannot be solved. According to the Wiscombe condition [42], the number of expansion coefficients for yielding convergent results is

$$N_{\text{Wis}}(k_\rho \rho) = k_\rho \rho + 4.05(k_\rho \rho)^{1/3} + 2. \tag{35}$$

When the size of scatterer or the number of scatterers increases, more expansion terms are needed to maintain the accuracy of the T-matrix algorithm.

REFERENCES

[1] K. Davies, *Ionospheric Radio*. London, U.K.: IET, 1990.

[2] K. Rawer, *Wave Propagation in the Ionosphere*, vol. 5. New York, NY, USA: Springer, 2013.

[3] S. A. Cummer, "Modeling electromagnetic propagation in the Earth-ionosphere waveguide," *IEEE Trans. Antennas Propag.*, vol. 48, no. 9, pp. 1420–1429, Sep. 2000.

[4] W. Utlaut, "An ionospheric modification experiment using very high power, high frequency transmission," *J. Geophys. Res.*, vol. 75, no. 31, pp. 6402–6405, 1970.

[5] T. Georges, "Amplification of ionospheric heating and triggering of 'spread f'by natural irregularities," *J. Geophys. Res.*, vol. 75, no. 31, pp. 6436–6438, 1970.

[6] D. Farley Jr., "A plasma instability resulting in field-aligned irregularities in the ionosphere," *J. Geophys. Res.*, vol. 68, no. 22, pp. 6083–6097, 1963.

[7] K. Cole, "Formation of field-aligned irregularities in the magnetosphere," *J. Atmos. Terr. Phys.*, vol. 33, no. 5, pp. 741–750, 1971.

[8] B. Inhester, A. Das, and J. Fejer, "Generation of small-scale field-aligned irregularities in ionospheric heating experiments," *J. Geophys. Res. Space Phys.*, vol. 86, no. A11, pp. 9101–9106, 1981.

[9] G. D. Thome and D. W. Blood, "First observations of rf backscatter from field-aligned irregularities produced by ionospheric heating," *Radio Sci.*, vol. 9, no. 11, pp. 917–921, 1974.

[10] N. Blagoveshchenskaya, T. Borisova, T. Yeoman, M. Rietveld, I. Ivanova, and L. Baddeley, "Artificial small-scale field-aligned irregularities in the high latitude F region of the ionosphere induced by an x-mode HF heater wave," *Geophys. Res. Lett.*, vol. 38, no. 8, 2011.

[11] M. Yamamoto, S. Fukao, R. F. Woodman, T. Ogawa, T. Tsuda, and S. Kato, "Mid-latitude e region field-aligned irregularities observed with the MU radar," *J. Geophys. Res. Space Phys.*, vol. 96, no. A9, pp. 15943–15949, 1991.

[12] T. Franz, M. Kelley, and A. Gurevich, "Radar backscattering from artificial field-aligned irregularities," *Radio Sci.*, vol. 34, no. 2, pp. 465–475, 1999.

[13] P. Fialer, "Field-aligned scattering from a heated region of the ionosphere–observations at HF and VHF," *Radio Sci.*, vol. 9, no. 11, pp. 923–940, 1974.

[14] G. Barry, "HF-VHF communications experiment using man-made field-aligned ionospheric scatterers," *Radio Sci.*, vol. 9, no. 11, pp. 1025–1032, 1974.

[15] L.-C. Tsai, F. Berkey, A. Wong, and J. Pau, "Dynasonde observations of ionospheric modification experiments with the HIPAS observatory," *J. Atoms. Sol.-Terr. Phys.*, vol. 63, no. 2-3, pp. 107–116, 2001.

[16] R. Lukianova, V. Frolov, and A. Ryabov, "First SWARM observations of the artificial ionospheric plasma disturbances and field-aligned currents induced by the SURA power HF heating," *Geophys. Res. Lett.*, vol. 46, no. 22, pp. 12731–12738, 2019.

[17] S. Kuo and A. Snyder, "Artificial plasma cusp generated by upper hybrid instabilities in HF heating experiments at HAARP," *J. Geophys. Res. Space Phys.*, vol. 118, no. 5, pp. 2734–2743, 2013.

[18] J. Minkoff, M. Laviola, S. Abrams, and D. Porter, "Radio frequency scattering from a heated ionospheric volume, 2, bistatic measurements," *Radio Sci.*, vol. 9, no. 11, pp. 957–963, 1974.

[19] J. Minkoff, P. Kugelman, and I. Weissman, "Radio frequency scattering from a heated ionospheric volume: 1, VHF/UHF field-aligned and plasma-line backscatter measurements," *Radio Sci.*, vol. 9, no. 11, pp. 941–955, 1974.

[20] J. Minkoff, "Radio frequency scattering from a heated ionospheric volume: 3, cross section calculations," *Radio Sci.*, vol. 9, no. 11, pp. 997–1004, 1974.

[21] L. Li-Bin, L. Qing-Liang, H. Shu-Ji, and W. Zhen-Sen, "Theoretical analysis of effects on high frequency vertical sounding by artificial field-aligned irregularities," *Acta Phys. Sin.*, vol. 66, no. 5, 2017, Art. no. 059401.

[22] N. Balan, L. Liu, and H. Le, "A brief review of equatorial ionization anomaly and ionospheric irregularities," *Earth Planet. Phys.*, vol. 2, no. 4, pp. 257–275, 2018.

[23] F. Deng, Z. Zhao, R. Shi, and Y. Zhang, "Two-dimensional simulation of high-frequency-induced large-scale irregularities in F region," *Acta Phys. Sin*, vol. 58, no. 10, pp. 7382–7390, 2009.

[24] E. Andreeva et al., "Radiotomography and HF ray tracing of the artificially disturbed ionosphere above the sura heating facility," *Radio Sci.*, vol. 51, no. 6, pp. 638–644, 2016.

[25] D. R. Smith, "An investigation of electromagnetic waves in the ocean and ionosphere using the finite-difference time-domain method," Ph.D. dissertation, The Univ. Utah, Salt Lake City, UT, USA, 2020.

[26] D. Smith, C. Huang, E. Dao, S. Pokhrel, and J. Simpson, "FDTD modeling of high-frequency waves through ionospheric plasma irregularities," *J. Geophys. Res. Space Phys.*, vol. 125, no. 3, 2020, Art. no. e2019JA027499.

[27] K. Niknam and J. Simpson, "A review of grid-based, time-domain modeling of electromagnetic wave propagation involving the ionosphere," *IEEE J. Multiscale Multiphys. Comput. Techn.*, vol. 6, pp. 214–228, 2021.

[28] H. Booker and W. Gordon, "A theory of radio scattering in the troposphere," *Proc. IRE*, vol. 38, no. 4, pp. 401–412, 1950.

[29] E. F. Knott, J. F. Schaeffer, and M. T. Tulley, *Radar Cross Section*. Raleigh, NC, USA: SciTech Publishing, 2004.

[30] W. C. Chew, *Waves and Fields in Inhomogenous Media*, vol. 16. Hoboken, NJ, USA: Wiley, 1999.
[31] P. Waterman, "Matrix formulation of electromagnetic scattering," *Proc. IEEE*, vol. 53, no. 8, pp. 805–812, Aug. 1965.
[32] W. Chew, "An N^2 algorithm for the multiple scattering solution of N scatterers," *Micro Opt. Technol. Lett.*, vol. 2, no. 11, pp. 380–383, 1989.
[33] W. C. Chew, L. Gurel, Y.-M. Wang, G. Otto, R. L. Wagner, and Q. H. Liu, "A generalized recursive algorithm for wave-scattering solutions in two dimensions," *IEEE Trans. Microw. Theory Techn.*, vol. 40, no. 4, pp. 716–723, Apr. 1992.
[34] W. Chew, Y. Wang, and L. Gürel, "Recursive algorithm for wave-scattering solutions using windowed addition theorem," *J. Electromagn. Waves Appl.*, vol. 6, no. 7, pp. 1537–1560, 1992.
[35] X. Ye, X. Chen, Y. Zhong, and R. Song, "Simultaneous reconstruction of dielectric and perfectly conducting scatterers via T-matrix method," *IEEE Trans. Antennas Propagat.*, vol. 61, no. 7, pp. 3774–3781, Jul. 2013.
[36] W.-Z. Yan, Y. Du, Z. Li, E.-X. Chen, and J.-C. Shi, "Characterization of the validity region of the extended T-matrix method for scattering from dielectric cylinders with finite length," *Prog. Electromagn. Res.*, vol. 96, pp. 309–328, 2009.
[37] C. Shuai, Z. Xiao-Juan, and F. Guang-You, "Investigation of the scattering characteristics from discrete random scatterers based on recursive aggregate t-matrix algorithm," *Acta Phys. Sin.*, vol. 63, no. 15, 2014, Art. no. 154202.
[38] Y. Yu, J. Niu, and J. J. Simpson, "A 3-D global earth-ionosphere FDTD model including an anisotropic magnetized plasma ionosphere," *IEEE Trans. Antennas Propag.*, vol. 60, no. 7, pp. 3246–3256, Jul. 2012.
[39] N. Cartwright and K. Oughstun, "Ultrawideband pulse propagation through a homogeneous, isotropic, lossy plasma," *Radio Sci.*, vol. 44, no. 04, pp. 1–11, 2009.
[40] D. Bilitza, "International reference ionosphere 2000," *Radio Sci.*, vol. 36, no. 2, pp. 261–275, 2001.
[41] A. V. Osipov and S. A. Tretyakov, *Modern Electromagnetic Scattering Theory With Applications*. Hoboken, NJ, USA: Wiley, 2017.
[42] J. R. Allardice and E. C. L. Ru, "Convergence of mie theory series: Criteria for far-field and near-field properties," *Appl. Opt.*, vol. 53, no. 31, pp. 7224–7229, 2014.